






Electric field induced parametric excitation of exchange magnons in a CoFeB/MgO junction

Angshuman Deka ^{1,*}, Bivas Rana ^{2,†}, Ryo Anami,¹ Katsuya Miura,³ Hiromasa Takahashi ³,
YoshiChika Otani ^{2,4} and Yasuhiro Fukuma ^{1,2,5,‡}

¹*Department of Physics and Information Technology, Kyushu Institute of Technology, 680-4 Kawazu, Iizuka 820-8502, Japan*

²*Center for Emergent Matter Science, RIKEN, 2-1 Hirosawa, Wako 351-0198, Japan*

³*Research and Development Group, Hitachi Ltd., 1-280 Higashi-koigakubo, Kokubunji 185-8601, Japan*

⁴*Institute for Solid State Physics, University of Tokyo, Kashiwa, Chiba 277-8581, Japan*

⁵*Research Center for Neuromorphic AI Hardware, Kyushu Institute of Technology, Kitakyushu 808-0196, Japan*



(Received 6 April 2021; revised 22 March 2022; accepted 23 March 2022; published 20 May 2022)

Inspired by the success of field-effect transistors in electronics, electric field controlled magnetization dynamics has emerged as an important ingredient in low-power spintronic devices. Here, we demonstrate electric field induced parametric excitation for CoFeB/MgO junctions by using interfacial in-plane magnetic anisotropy (IMA). When the IMA and the external magnetic field are parallel to each other, magnons are efficiently excited by electric field induced parametric resonance. The corresponding wavelengths are estimated to be tuned down to exchange interaction length scales by changing the input power and frequency of the applied voltage. A generalized phenomenological model is developed to explain the underlying role of the electric field torque. Electric field control of IMA is shown to be the origin for excitation of both uniform and parametric resonance modes in the in-plane magnetized sample, a crucial element for purely electric field induced magnetization dynamics. Electric field excitation of exchange magnons, with no Joule heating, offers a good opportunity for developing nanoscale magnonic devices and exploring various nonlinear dynamics in nanomagnetic systems.

DOI: [10.1103/PhysRevResearch.4.023139](https://doi.org/10.1103/PhysRevResearch.4.023139)

I. INTRODUCTION

Nonlinear dynamics in magnetic systems have attracted considerable attention from a fundamental research standpoint, as well as for applications in reservoir computing [1–3]. Interaction among spins in magnetic materials is intrinsically nonlinear, which gives rise to several phenomena such as harmonic oscillation and auto-oscillation in magnetically excited states [4,5]. The collective excitation of spins gives rise to propagating spin wave modes, whose quanta are known as magnons, that carry angular momentum. Therefore, the spin wave is also useful for generating spin current [6–8]. Magnetic insulators, such as Y₃Fe₅O (YIG), are considered excellent materials for studying the nonlinearity in magnetization dynamics due to their small magnetic damping. However, compatibility of such insulating magnets with computing technology is limited by the fact that high-quality garnets

are typically grown on Gd₃Ga₅O substrates, whereas existing complementary metal-oxide semiconductor (CMOS) technology uses metallic thin films grown on Si substrates. Therefore, the ability to excite and control nonlinear dynamics in metallic ferromagnets such as CoFeB is considered a promising avenue toward realizing spintronic devices that are compatible with CMOS processes.

Reports on nonlinear parametric excitation in insulating ferromagnets, like YIG, far exceed those of their metallic counterparts because of lower linewidths of resonant spectra and hence lower threshold power for exciting nonlinear dynamics [9–11]. Recent discoveries in the field of spintronics such as spin-transfer torque [12,13], spin-orbit torque [14] and electric field torque [15] have provided unique insight towards studying nonlinear dynamics in magnetic systems. The electric field torque, originating from voltage controlled magnetic anisotropy (VCMA) at ferromagnetic metal-oxide interfaces, allows us to control the magnetization without Joule heating [15–18]. The parametric excitation using VCMA was theoretically predicted [19] and then experimentally realized using magnetic tunnel junctions with an MgO tunneling layer [20]. VCMA originates from selective electron-hole doping in the 3d orbitals of the interfacial ferromagnetic atoms in the presence of an electric field [21,22]. Therefore, electric field torque on the magnetization arises due to a modulation of the interfacial perpendicular magnetic anisotropy (PMA) [23–28]. The torque is proportional to $(dH_p/dV)V \sin\theta \cos\theta$: modulation of the PMA field H_p per unit voltage V , i.e., $(dH_p/dV)V$, and orientation of magnetization, i.e., θ , the elevation angle of the magnetization from the film plane.

*Present address: Birck Nanotechnology Center, School of Electrical and Computer Engineering, Purdue University, West Lafayette, Indiana 47907, USA.

†Present address: ISQI, Faculty of Physics, Adam Mickiewicz University, Uniwersytetu Poznańskiego 2, Poznań 61–614, Poland.

‡fukuma@phys.kyutech.ac.jp

Published by the American Physical Society under the terms of the [Creative Commons Attribution 4.0 International license](https://creativecommons.org/licenses/by/4.0/). Further distribution of this work must maintain attribution to the author(s) and the published article's title, journal citation, and DOI.

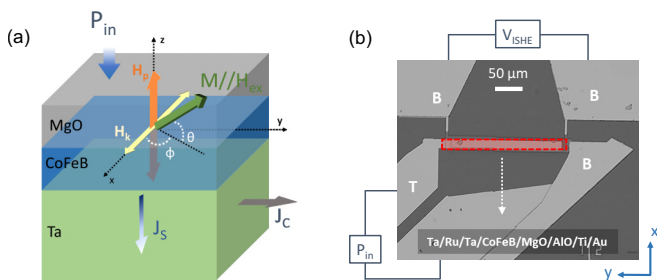


FIG. 1. (a) Schematic showing the orientation of the perpendicular magnetic anisotropy field H_p and in-plane magnetic anisotropy field H_k . Magnetization M is taken parallel to magnetic field H_{ex} applied at an elevation angle θ and azimuthal angle ϕ . A microwave voltage is applied at the CoFeB/MgO junction using an input power P_{in} . Spin current J_s is pumped and then converted into charge current J_c due to inverse spin Hall effect of the Ta layer. (b) Optical image of the sample used in this paper. The top electrode on MgO is marked as T, and the bottom electrodes of the Ta layer are marked as B. The rectified voltage from J_c , i.e., V_{ISHE} , is detected across the Ta/Ru/Ta underlayer.

Note that the torque on the magnetization is zero for in-plane ($\theta = 0^\circ$) and perpendicular ($\theta = 90^\circ$) magnetized ferromagnetic thin films. To overcome this limitation, the interfacial magnetic anisotropy of CoFeB/MgO junctions can be tuned by magnetic annealing [29], which allows us to control the symmetry of the electric field torque via VCMA [see Eq. (2)]. In this paper, we demonstrate electric field induced magnetization dynamics for an in-plane magnetized CoFeB layer by using VCMA of in-plane magnetic anisotropy (IMA) induced by magnetic annealing. The parallel pumping configuration, in which the microwave driving field, generated by voltage-controlled IMA, is applied parallel to the external field, has lower critical fields of nonlinear magnetization dynamics which can then excite various magnons. The applied power dependence of magnons is studied to gain insight into the dynamical processes. Finally, a phenomenological model is developed to confirm the role of the electric field torque via VCMA of IMA in excitation of the magnetization dynamics.

II. METHODS

Multilayer stacks of Ta(5)/Ru(10)/Ta(5)/Co₂₀Fe₆₀B₂₀(1.8)/MgO(2)/Al₂O₃(10), (numbers in parentheses are thicknesses in nm), were sputtered at room temperature onto thermally oxidized Si (100) substrates. The multilayer stack was patterned into rectangles of length (l) 250 μm and width (w) 20 μm by photolithography and Ar⁺ ion milling. Au electrodes were fabricated by lift-off processes. After device fabrication, the samples were annealed with a 0.7 T magnetic field along the shorter axis of the rectangle (x axis, $\theta = \phi = 0^\circ$) to induce an IMA. Magnetization dynamics are excited by applying an AC voltage which modulates H_p and H_k of the CoFeB/MgO junction, as shown schematically in Fig. 1(a). Uniform ferromagnetic resonance (FMR) and magnons can generate spin current toward an adjacent Ta layer via spin pumping, and the injected spin current can be detected using the inverse spin Hall effect (ISHE). The ISHE voltage V_{ISHE} was detected by a standard lock-in detection technique. The

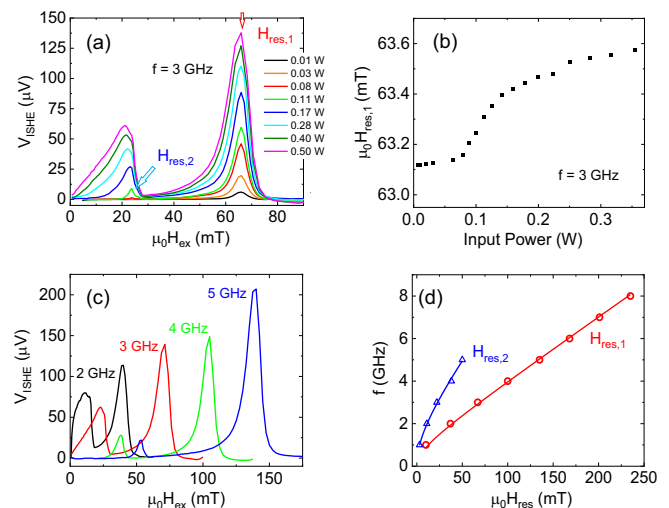


FIG. 2. (a) Inverse spin Hall voltage V_{ISHE} as a function of external magnetic field H_{ex} for different input powers P_{in} at a frequency $f = 3$ GHz, when H_{ex} is applied along $\theta = \phi = 0^\circ$. (b) Resonance field $H_{res,1}$ of the ferromagnetic resonance mode as a function of P_{in} at $f = 3$ GHz. (c) V_{ISHE} spectra, at high power $P_{in} = 0.3$ W, for $f = 2$ –5 GHz. (d) f as a function of H_{res} (for $H_{res,1}$ and $H_{res,2}$). The experimental data are fitted with the Kittel equation (lines).

amplitude of the input microwave is modulated at a reference frequency of 79 Hz. The DC rectified voltage is detected across the two ends of the Ta strip [bottom electrodes marked on the upper side in Fig. 1(b)] using a lock-in amplifier. We obtained $\mu_0 H_p = 1405$ mT and $\mu_0 H_k = 2.5$ mT for PMA and IMA, respectively, from ϕ -dependent V_{ISHE} measurements (see Appendix A). All measurements are performed at room temperature.

III. RESULTS AND DISCUSSION

Figure 2(a) shows V_{ISHE} spectra as a function of input power P_{in} at frequency $f = 3$ GHz when H_{ex} is applied along $\theta = \phi = 0^\circ$. For $P_{in} < 0.08$ W, we observe a single peak around $\mu_0 H_{ex} = 63$ mT ($H_{res,1}$) in the V_{ISHE} spectrum. As $P_{in} > 0.08$ W, we observe the emergence of a second peak around $\mu_0 H_{ex} = 23$ mT ($H_{res,2}$). Figure 2(b) shows the dependence of $H_{res,1}$ on P_{in} . Above $P_{in} \sim 0.08$ W, $H_{res,1}$ starts to shift. Interestingly, this shift of ~ 0.5 mT is significantly smaller than that obtained for our control sample where the shift is ~ 3.6 mT when FMR is excited using a z -axial Oersted field (see Appendix B). A second peak also appears at $H_{res,2}$ above $P_{in} \sim 0.08$ W, indicating the onset of parametric resonance excitation. The V_{ISHE} spectrum at $P_{in} = 0.3$ W for different applied microwave frequencies is shown in Fig. 2(c). Here, $H_{res,1}$ and $H_{res,2}$ both increase with increasing frequency and are fitted to the Kittel formula $f = \gamma \sqrt{H_{res,1}(H_{res,1} + M_{eff})}$ and $\frac{f}{2} = \gamma \sqrt{H_{res,2}(H_{res,2} + M_{eff})}$, respectively, with γ the gyromagnetic ratio whose value is estimated to be 0.0298 GHz mT⁻¹ [29] and μ_0 the permeability of free space. The effective demagnetizing field $M_{eff} (= M_s - H_p)$ is estimated to be 95 mT. The rectified voltages at $H_{res,1}$ and $H_{res,2}$ correspond to the uniform FMR mode and the parametric magnon mode, respectively.

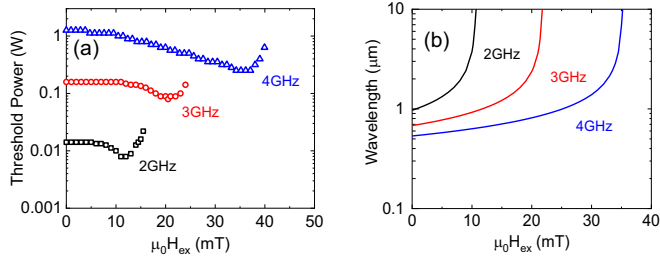


FIG. 3. (a) Threshold power of parametric excitation modes as a function of H_{ex} for $f = 2\text{--}4$ GHz. (b) Corresponding magnon wavelengths, calculated using Eq. (1), as a function of H_{ex} for $f = 2\text{--}4$ GHz.

The threshold power of the parametric excitation as a function of the external magnetic field was measured (see Appendix C), as shown in Fig. 3(a). We can see the lowest threshold power at $H_{\text{ex}} \sim H_{\text{res},2}$ and the butterfly curve well known in the nonlinear magnetization dynamics reported for YIG and NiFe [30–32]. In the linear excitation regime, the cone angle of the magnetization precession is small enough to consider M_{eff} to be constant, and therefore, no change of $H_{\text{res},1}$ is observed in the P_{in} dependence, as can be seen in Fig. 2(b). However, in the nonlinear excitation regime, a large angle of precession causes a change of M_{eff} , evident from $H_{\text{res},1}$ which varies with P_{in} , as observed in metallic NiFe [33] and insulating YIG [34] earlier. The magnetization component parallel to the effective field, i.e., m_x , oscillates (δm_x) at a frequency twice that of the transverse components [35]. This can directly couple with a modulation of H_k via VCMA, the so-called parallel pumping, which shows a minimum of the threshold power at $H_{\text{ex}} \sim H_{\text{res},2}$. As P_{in} increases, various magnon modes are excited for $H_{\text{ex}} < H_{\text{res},2}$. We can calculate the corresponding wavelength λ as a function of H_{ex} using the relation [36]:

$$\lambda = \left[\frac{M_{\text{eff}}}{2\gamma A} \left(\sqrt{\left(\frac{f}{2}\right)^2 + \left(\frac{\gamma M_{\text{eff}}}{2}\right)^2} - \gamma \left(H_{\text{ex}} + \frac{M_{\text{eff}}}{2} \right) \right) \right]^{-0.5}. \quad (1)$$

Figure 3(b) shows the H_{ex} vs λ plot for the sample in this paper. The estimated values of λ in the low H_{ex} region are two orders smaller than the lateral excitation length scales, well into the exchange-interaction regime for magnons which becomes predominant at $\lambda < 1 \mu\text{m}$. The wavelength and wave number can be tuned by changing the input power and frequency of the applied voltage. The drastic increase in threshold power for $H_{\text{ex}} > H_{\text{res},2}$ is because no magnon mode exists in this region.

Subsequently, we study the power dependence of the voltage amplitudes to gain insight into the processes driving the magnons. Figures 4(a) and 4(b) show the dependence of the magnitude of V_{ISHE} on P_{in} at $\mu_0 H_{\text{ex}} = 31, 11.5, 6,$ and 3 mT for $f = 2$ GHz and at $\mu_0 H_{\text{ex}} = 63.1, 20.5, 10,$ and 5 mT for $f = 3$ GHz, respectively. In the low P_{in} region, V_{ISHE} of the FMR mode ($\mu_0 H_{\text{ex}} = 31$ and 63.1 mT) increases linearly with increasing P_{in} , and no broadening of the V_{ISHE} peak was observed, implying that the magnetization dynamics follows

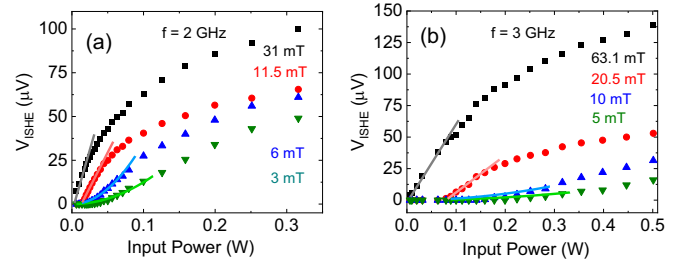


FIG. 4. Amplitude of V_{ISHE} as a function of input power P_{in} , for different H_{ex} , at frequencies (a) 2 GHz and (b) 3 GHz. Gray and red lines are linear fits to P_{in} , while blue and green lines are quadratic fits to P_{in} .

the Landau-Lifshitz-Gilbert equation with a constant damping term, in the linear excitation regime. As P_{in} increases further, an additional peak due to the excitation of parametric resonance can be observed around $\mu_0 H_{\text{ex}} = 11.5$ and 20.5 mT for $f = 2$ and 3 GHz, respectively. Note that V_{ISHE} of the parametric excitation mode increases linearly with increasing P_{in} in the low power region, as seen in Fig. 4. VCMA of H_k , which is parallel to the external magnetic field, can directly couple with a quasi-uniform mode at $2f$, so-called parallel pumping, and therefore, V_{ISHE} increases linearly with P_{in} , which can be attributed to a monotonic increase in the amplitude of δm_x . In the high P_{in} region, such a linear behavior for the parametric excitation mode is suppressed, and nonzero V_{ISHE} at low magnetic fields [$\mu_0 H_{\text{ex}} = 6$ and 3 mT in Fig. 4(a) and 10 and 5 mT in Fig. 4(b)] are observed. This behavior can be understood in terms of energy transfer from the parametric mode to higher-order magnon modes, in which the threshold power of the instabilities is determined by competition between the mode-coupling efficiency and the magnon linewidth [37]. The coupling efficiency of the parametric excitation mode scales with the square of its amplitude [30], and therefore, V_{ISHE} increases as a function of the square of P_{in} . As P_{in} increases further, there is a deviation from linear dependence. This can be attributed to the scaling of the voltages as a function of the square root of the power because of the temperature independence of parametric instabilities [20]. We note that, in our samples, such a deviation from linear dependence at high input power may also be due to Joule heating and magnon-magnon scattering which increases the magnon linewidth.

To understand the contribution of VCMA to magnetization dynamics in the samples, we develop a phenomenological model of V_{ISHE} . The torque arising from VCMA of both H_p and H_k can be estimated as below (see Appendix D):

$$\tau_{\text{VCMA}} \propto \begin{bmatrix} -\frac{\partial H_p}{\partial V} V_{\text{rf}} \sin \varphi \sin \theta \cos \theta \\ \left(\frac{\partial H_p}{\partial V} - \frac{\partial H_k}{\partial V} \right) V_{\text{rf}} \cos \varphi \sin \theta \cos \theta \\ \frac{\partial H_k}{\partial V} V_{\text{rf}} \sin \varphi \cos \varphi \cos^2 \theta \end{bmatrix}, \quad (2)$$

where $\partial H_p / \partial V$ and $\partial H_k / \partial V$ represent the voltage dependence of anisotropy fields H_p and H_k , respectively, and V_{rf} is the amplitude of AC voltage applied at the CoFeB/MgO junction. From a theoretical model, rectified voltage of V_{ISHE} is given by $V_{\text{ISHE}} = A' \theta_c^2 \cos \varphi \cos \theta$ [38–40]. Here, θ_c is the cone angle of the magnetization precession and $A' = -\frac{\theta_{\text{SH}} e \zeta f \lambda_{\text{sd}} L_{\text{NM}} g^{\uparrow\downarrow}}{\sigma_{\text{NM}} \mu_{\text{NM}}} \tanh\left(\frac{t_{\text{NM}}}{2\lambda_{\text{sd}}}\right)$, where e , $g^{\uparrow\downarrow}$, ζ , θ_{SH} , λ_{sd} , σ_{NM} ,

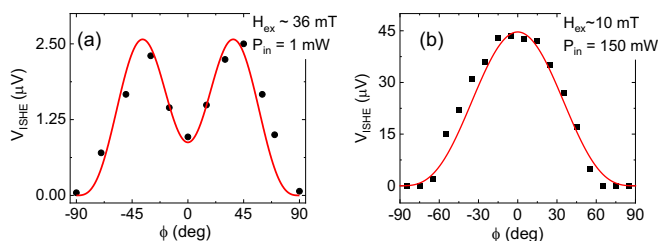


FIG. 5. (a) Dependence of V_{ISHE} amplitude on azimuthal angle ϕ , at $\mu_0 H_{\text{ex}} = 36$ mT, for input power $P_{\text{in}} = 0.001$ W and $f = 2$ GHz. The experimental data are fitted with Eq. (4). (b) Dependence of V_{ISHE} amplitude on azimuthal angle ϕ , at $\mu_0 H_{\text{ex}} = 11.5$ mT, for input power $P_{\text{in}} = 0.280$ W and $f = 2$ GHz. The experimental data are fitted with $\cos^3 \phi$.

L_{NM} , and t_{NM} are the charge of an electron, spin mixing conductance of the Ta/CoFeB interface, correction factor arising from elliptical precession trajectories, spin Hall angle, spin diffusion length, conductivity, length, and thickness of the Ta layer, respectively. In our analysis of the angular dependence of the uniform FMR mode, since our H_p is almost equal to the demagnetizing field, we can approximate the $\zeta \sim 1$ [35]. In the linear excitation regime, $\theta_c = \eta\tau$, we can obtain the following expression of V_{ISHE} for the electric field torques:

$$V_{\text{ISHE,VCMA}} = AV_{\text{rf}}^2 \left\{ \left(\frac{\partial H_p}{\partial V} \sin \varphi \sin \theta \right)^2 + \left[\left(\frac{\partial H_p}{\partial V} - \frac{\partial H_k}{\partial V} \right) \cos \varphi \sin \theta \right]^2 + \left(\frac{\partial H_k}{\partial V} \sin \varphi \cos \varphi \cos \theta \right)^2 \right\} \cos \varphi \cos^3 \theta, \quad (3)$$

where $A = A'\eta^2$, and η is a constant of proportionality correlating θ_c and τ . The application of a microwave voltage in the sample gives rise to an induced current, which causes h_{rf} [23]. Therefore, in our analysis, we should consider Oersted field torques to be caused by $h_{\text{rf},x}$, $h_{\text{rf},y}$, and $h_{\text{rf},z}$, and so we performed finite element method (FEM) analysis using COMSOL multiphysics simulator (see Appendix E). It reveals the presence of x - and y -axial Oersted fields arising from an induced current, while the z -axial Oersted field is zero. Further, for the samples used in this paper, which have $l : w = 12 : 1$, the Oersted field along the shorter in-plane dimension is very small compared with that oriented along the longer one, i.e., $h_{\text{rf},x} \ll h_{\text{rf},y}$. As a result, the in-plane angle dependence ($\theta = 0^\circ$) of V_{ISHE} can be obtained as follows:

$$V_{\text{ISHE},\varphi} = a \left[4 \left(\frac{\partial H_k}{\partial V} V_{\text{rf}} \right)^2 \sin^2 \varphi + h_{\text{rf},y}^2 \right] \cos^3 \varphi, \quad (4)$$

where $a = A/4$.

Figure 5(a) shows V_{ISHE} as a function of ϕ for the FMR mode. While the Oersted field torque, arising from $h_{\text{rf},y}$, gives us a maxima at $\phi = 0^\circ$, the electric field torque, via VCMA of H_k , gives us a maxima at an angle between $\phi = 0^\circ$ and 90° . Therefore, an increase of V_{ISHE} at $\phi = 40^\circ$ in Fig. 5(a) suggests that the electric field torque gives rise to the FMR mode. The experimental data are fitted using Eq. (4) with the values $a \left(\frac{\partial H_k}{\partial V} V_{\text{rf}} \right)^2 = 2.87$ and $ah_{\text{rf},y}^2 = 0.88$. The contribution

of $h_{\text{rf},y}$ can be understood to arise from an impedance mismatch between the sample and the 50Ω signal line. As the frequency increases, the VCMA efficiency decreases and the Oersted field contribution increases because the sample shows a capacitive nature (see Appendix F). This was confirmed by performing the angular dependences at different frequencies; we obtained values $a \left(\frac{\partial H_k}{\partial V} V_{\text{rf}} \right)^2 = 0.90$ and $ah_{\text{rf},y}^2 = 0.65$ for $f = 4$ GHz (see Appendix G). In this paper, at $P_{\text{in}} = 0.001$ W, we confirm that the electric field torque is higher than the Oersted field torque up to applied microwave frequency ~ 4 GHz.

In addition to the uniform FMR mode, we studied the torque contribution of the parametric excitation. Figure 5(b) shows V_{ISHE} as a function of ϕ at $\mu_0 H_{\text{ex}} = 11.5$ mT for $f = 2$ GHz. The amplitude can be fitted using a $\cos^3 \phi$ function, which is different from the FMR mode. This behavior is well understood by considering the parallel pumping mechanism. VCMA of H_k can directly couple with the quasi-uniform mode with $2f$, and thus, its torque is obtained to be a function of $\cos \phi$. As discussed previously, assuming the precession angle θ_c is proportional to its torque, V_{ISHE} is proportional to θ_c^2 and thus to $\cos^2 \phi$. The product of this with the detection efficiency of ISHE, which is proportional to $\cos \phi$, gives us $\cos^3 \phi$, which is used for fitting to the experimental data. A similar angular dependence is obtained for other frequencies. For the parametric excitation, two mechanisms can be considered: one is parallel pumping [30], and the other is the first-order Suhl instability via the FMR mode [41]. As mentioned above, the parallel pumping field can be directly coupled with the magnon mode, and therefore, the critical field of the parametric excitation is much lower than that of the first-order process. In fact, no magnon with $k \neq 0$ is excited by the Oersted field torque of $h_{\text{rf},z}$ in our control sample that can give rise to only a perpendicular pumping mechanism (see Appendix B). To summarize, in Figs. 2–4, when H_{ex} is along the x axis, although the uniform FMR mode is excited by the Oersted field $h_{\text{rf},y}$, the excitation of exchange magnons via parametric resonance can only be explained using a parallel pumping mechanism, i.e., VCMA of H_k .

IV. CONCLUSIONS

In conclusion, we have demonstrated the excitation of magnetization dynamics in CoFeB/MgO junctions by the electric field torque via VCMA. The interfacial magnetic anisotropies allow us to excite not only uniform FMR modes but also parametric modes for the in-plane magnetized CoFeB layer. More importantly, through the VCMA of IMA, parallel pumping enables us to reach critical fields at lower powers for the nonlinear excitation and to couple effectively with various magnon modes. This allows us to tune its wavelengths down to exchange interaction length scales. Magnetoelectric effects in ferromagnetic metal-oxide junctions are reported through other mechanisms such as reversible oxidation [42] and piezoelectricity [43], in addition to VCMA. The advantage of VCMA lies in its compatibility with existing CMOS technologies that operate in the gigahertz regime, whereas the former effects operate only in the kilohertz regime. Therefore, the electric field torque effects demonstrated in this paper are useful toward development of spintronic computing technologies, particularly magnonic logic devices [44].

ACKNOWLEDGMENTS

We would like to thank K. Kondou for helpful discussions. This paper was supported by Grants-in-Aid (No. 26103002, No. 16K18079, and No. 18H01862) from JSPS and Materials Science Foundation, Hitachi Metals. B.R. acknowledges RIKEN Incentive Research Project Grant No. FY2019.

APPENDIX A: ESTIMATION OF MAGNETIC ANISOTROPY FIELDS IN THE CoFeB/MgO JUNCTION

The angular-dependent FMR measurement is an efficient technique to accurately estimate magnetic anisotropy in ferromagnetic thin films [29,45] compared with that estimated from magnetic hysteresis measurements. This is especially true when the magnetic anisotropy field is significantly lower than the demagnetizing field. The FMR measurements should be performed at low input power to eliminate nonlinear magnetization dynamics that cause a change in demagnetizing field in the sample. This can enable us to estimate anisotropy fields down to a few Oersteds [45]. Here, to estimate the values of in-plane and PMA fields, i.e., H_k and H_p , respectively, we measured the dependence of rectified voltage V_{ISHE} on the in-plane azimuthal angle ϕ . The input power of the applied microwave is 0.001 W. The FMR spectra were fitted using the Lorentzian function, as shown in Fig. 6(a). From the fitting, we can estimate the resonance field $H_{\text{res},1}$ as a function of ϕ , as shown in Fig. 6(b). The data are then fitted using the following equation [29]:

$$H_{\text{res},1} = -H_k + \frac{3}{2}H_k \sin^2 \phi - \frac{(M_s - H_p)}{2} + \frac{1}{2} \left[H_k^2 \sin^4 \phi + (M_s - H_p)^2 + 2(M_s - H_p)H_k \sin^2 \phi + 4 \left(\frac{f}{\mu_0 \gamma} \right)^2 \right]^{1/2}, \quad (\text{A1})$$

where M_s is the saturation magnetization, γ is the gyromagnetic ratio, and μ_0 the permeability of free space. From this fitting, we can estimate $\mu_0 H_p$ and $\mu_0 H_k$ are 1405 mT and 2.5 ± 0.2 mT, respectively, in the samples.

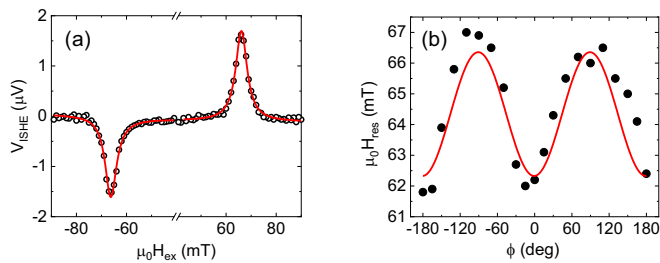


FIG. 6. (a) Inverse spin Hall effect voltage V_{ISHE} spectrum at $f = 3$ GHz for an in-plane H_{ex} along $\phi = 40$ degree. The experimental data are fitted with Lorentzian function (line) to obtain $H_{\text{res},1}$. (b) Azimuthal angle ϕ dependence of $H_{\text{res},1}$ for $f = 3$ GHz. Sinusoidal dependence shows the presence of an in-plane anisotropy in addition to the perpendicular magnetic anisotropy. The experimental data are fitted with Eq. (A1) (line) to obtain H_k and H_p .

APPENDIX B: INVERSE SPIN HALL VOLTAGE MEASUREMENTS USING COPLANAR WAVEGUIDE

We performed an in-plane angle-dependent measurement of the rectified voltage to determine the origin of the rectified voltage in the Ta/Ru/Ta/CoFeB/MgO multilayer stacks. The samples used in this measurement are like those used in our previous study [29]. Figure 7(a) shows the schematic of the setup used for detecting the rectified voltage. FMR is excited by a z -axial microwave field $h_{\text{rf},z}$ that is generated due to a charge current flowing in a nearby coplanar waveguide. According to Harder *et al.* [46], in this setup, anisotropic magnetoresistance (AMR) and anomalous Hall effect (AHE) of the ferromagnet show Lorentzian and dispersive line shapes, respectively, and spin pumping-ISHE (SP-ISHE) shows Lorentzian line shape. However, the AMR and ISHE spectra show a different symmetry as a function of in-plane angle ϕ . While the rectified voltage originating from AMR shows a $\sin 2\phi$ dependence, the SP-ISHE signal shows a $\cos \phi$ dependence. Figure 7(b) shows the rectified voltage in the sample. We can see a clear Lorentzian component in the spectrum. Figure 7(c) shows the angular-dependent values for the Lorentzian component of the rectified voltage, which indicates a $\cos \phi$ dependence. This allows us to eliminate the possibility of AMR and AHE in our multilayer stacks and confirm that the rectified voltage originates from ISHE.

We measured the dependence of the V_{ISHE} spectra for the sample on the input power via the Oersted field torque excitation. Figure 7(d) shows typical power-dependent V_{ISHE} spectra at $f = 3$ GHz and $\phi = \theta = 0^\circ$. In this configuration, $h_{\text{rf},z}$ excites FMR mode with a maximum torque, as can be seen in Eq. (D7). Figure 7(e) shows V_{ISHE} as a function of input power P_{in} , which confirms that the sample enters the nonlinear excitation regime at $P_{\text{in}} > 0.07$ W. However, no peak can be observed in Fig. 7(d) for the parametric excitation process. This indicates that perpendicular pumping shows a high threshold power of the parametric excitation of the sample.

APPENDIX C: ESTIMATION OF THRESHOLD POWER FOR PARAMETRIC EXCITATION PROCESS

To estimate the threshold power for parametric pumping via electric field torque, the V_{ISHE} spectra are measured as a function of P_{in} with an increment of 0.5 dBm, as shown in Fig. 8. For P_{in} up to 8.5 dBm (i.e., 7.1 mW), we observe only one peak for the FMR mode, as shown in Fig. 8(a). The background signal in the spectra is ~ 6 μV for $P_{\text{in}} = 8.5$ dBm and increases to 15 μV at $P_{\text{in}} = 11.5$ dBm (i.e., 14.1 mW). The spectra presented in Fig. 8 have been vertically translated by subtracting the background signal. At $P_{\text{in}} = 9.0$ dBm (i.e., 7.9 mW), in addition to the FMR peak at $\mu_0 H_{\text{ex}} \sim 36$ mT, we observe a new peak of the V_{ISHE} spectrum around $\mu_0 H_{\text{ex}} \sim 12$ mT, as shown in Fig. 8(b). This value of P_{in} is taken as the threshold power for $\mu_0 H_{\text{ex}} \sim 12$ mT. The parametric peak broadens with increasing P_{in} , thereby allowing us to obtain the threshold for other values of H_{ex} . As P_{in} increases to 11.5 dBm (i.e., 14.1 mW), we can obtain peaks for $0 \text{ mT} < \mu_0 H_{\text{ex}} < 15$ mT in the spectra, as shown in Fig. 8(f). Using this process,

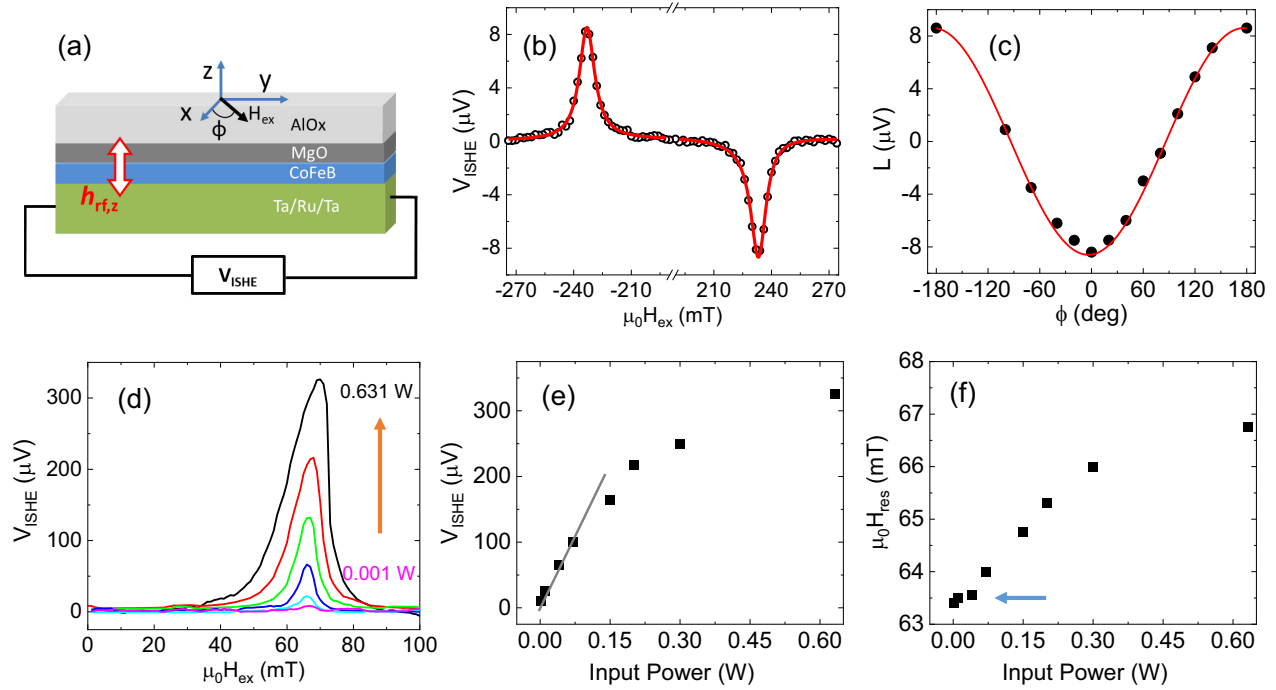


FIG. 7. (a) Experimental setup used for detecting rectified voltage across heavy metal underlayer. A z -axial microwave field $h_{rf,z}$ is generated by a coplanar waveguide near the multilayer strip, and a magnetic field H_{ex} is applied in the in-plane direction. (b) Rectified voltage spectra (circles) obtained for a microwave frequency of 8 GHz. Lines are fits to the experimental data using the Lorentzian function. (c) Amplitude of the Lorentzian L component (circles) as a function of in-plane azimuthal angle ϕ , fitted (line) using $\cos\phi$. (d) Typical V_{ISHE} spectra for different input power P_{in} ranging from 0.001 to 0.631 W ($f = 2$ GHz). (e) V_{ISHE} amplitudes and (f) resonance field H_{res} as a function of the input power. Linear fit (gray line) to the experimental data in Fig. 7(e) implies a linear excitation regime, and the arrow in Fig. 7(f) indicates the transition from linear to nonlinear excitation regime.

the values of the threshold power are plotted as a function of H_{ex} in Fig. 3(a).

APPENDIX D: INVERSE SPIN HALL VOLTAGE OF THE CoFeB/MgO JUNCTION

The torque on the magnetization in ferromagnets can be estimated using the relation $\tau \propto \hat{m} \times H_{eff}$, where \hat{m} is the unit magnetization vector with components $(\cos\theta\cos\phi, \cos\theta\sin\phi, \text{and } \sin\theta)$, and H_{eff} is the effective magnetic field given by the

differential of magnetic free energy F as follows:

$$H_{eff} = \frac{1}{\mu_o M} \frac{\partial F}{\partial \hat{m}}. \quad (D1)$$

The generalized expression of F can be written as the sum of magnetic anisotropy, demagnetizing, and Zeeman energies. For the sake of simplicity, we consider only the terms that have a time-dependent characteristic as follows:

$$F = \frac{\mu_o M_S}{2} \left(-\frac{\partial H_p}{\partial V} V_{rf} m_z^2 - \frac{\partial H_k}{\partial V} V_{rf} m_x^2 + h_{rf,x} m_x + h_{rf,y} m_y + h_{rf,z} m_z \right), \quad (D2)$$

where $\frac{\partial H_p}{\partial V} V_{rf}$ and $\frac{\partial H_k}{\partial V} V_{rf}$ are the voltage modulated parts of H_p and H_k , respectively, $h_{rf,x}$, $h_{rf,y}$, and $h_{rf,z}$ are the x -, y -, and z -axial microwave fields and m_x , m_y , and m_z are the x , y , and z components of \hat{m} , respectively. Due to the effect of the electric field on the anisotropy fields, we can assume the anisotropy fields as the sum of $H_{ani} = (H_{ani})_{V=0} + \frac{\partial H_{ani}}{\partial V} V_{rf}$, where the first term on the right is the anisotropy in the unbiased condition, i.e., $V = 0$, while the second term accounts for the voltage modulated increase or decrease of H_p or H_k due to a microwave voltage V_{rf} . Using Eq. (D1) and the VCMA terms of Eq. (D2), we can estimate the torque arising from VCMA

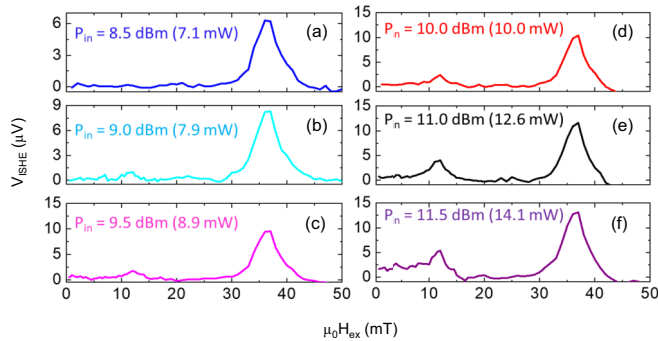


FIG. 8. (a)–(f) Typical V_{ISHE} spectra at $f = 2$ GHz for different values of input power P_{in} ranging from 8.5 to 11.5 dBm. Magnetization is oriented along the x axis by applying H_{ex} along $\theta = \phi = 0^\circ$.

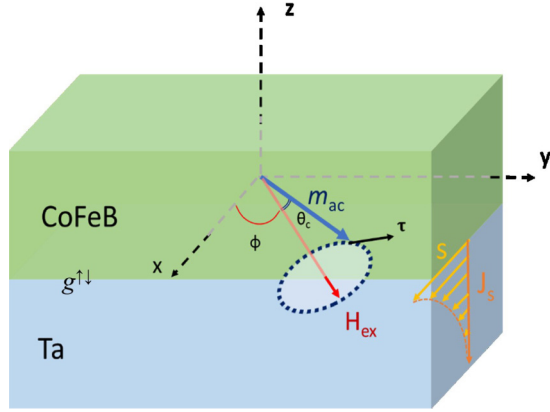


FIG. 9. Schematic to show the quantities described in the derivation. In the experiment, the external magnetic fields H_{ex} are applied in the film plane (elevation angle $\theta = 0^\circ$). Due to voltage controlled magnetic anisotropy (VCMA) or Oersted fields, there will be a torque τ on the magnetization. As a result, it will oscillate m_{ac} around H_{ex} during resonance, with a cone angle θ_c . Spin current J_s with a polarization s is pumped into the Ta layer from the CoFeB layer, which decays as it enters deeper inside the Ta layer. This decay (dashed orange curve) is characterized by the spin diffusion length λ_{sd} .

of both H_p and H_k as

$$\tau_{\text{VCMA}} \propto \begin{bmatrix} -\frac{\partial H_p}{\partial V} V_{\text{rf}} \sin \varphi \sin \theta \cos \theta \\ \left(\frac{\partial H_p}{\partial V} - \frac{\partial H_k}{\partial V} \right) V_{\text{rf}} \cos \varphi \sin \theta \cos \theta \\ \frac{\partial H_k}{\partial V} V_{\text{rf}} \sin \varphi \cos \varphi \cos^2 \theta \end{bmatrix}. \quad (\text{D3})$$

Due to the voltage modulation of H_k , we can have a nonzero torque on the magnetization even when it is oriented in the film plane ($\theta = 0^\circ$). Such a torque is not possible from the voltage modulation of H_p .

From the theory of spin pumping, the DC component of ISHE voltage V_{ISHE} in our device geometries is given by $V_{\text{ISHE}} = A\theta_c^2 \cos \varphi \cos \theta$. Here, θ_c is the precession cone

angle, and $A = -\frac{\theta_{\text{SH}} e f \lambda_{\text{sd}} L_{\text{NM}} g^{\uparrow\downarrow}}{\sigma_{\text{NM}} t_{\text{NM}}} \tanh\left(\frac{t_{\text{NM}}}{2\lambda_{\text{sd}}}\right)$, e being the charge of an electron, and $g^{\uparrow\downarrow}$ is the spin mixing conductance of the CoFeB/Ta interface. These quantities are represented schematically in Fig. 9. The precession cone angle is strongly dependent on the torque on the magnetization. Assuming a linear relationship between the two in the linear excitation regime, i.e., $\theta_c = \eta\tau$, we can obtain the following expression for the angular-dependent behavior if V_{ISHE} originates from the electric field induced FMR:

$$V_{\text{ISHE,VCMA}} = AV_{\text{rf}}^2 \left\{ \left(\frac{\partial H_p}{\partial V} \sin \varphi \sin \theta \right)^2 + \left[\left(\frac{\partial H_p}{\partial V} - \frac{\partial H_k}{\partial V} \right) \cos \varphi \sin \theta \right]^2 + \left(\frac{\partial H_k}{\partial V} \sin \varphi \cos \varphi \cos \theta \right)^2 \right\} \cos \varphi \cos^3 \theta. \quad (\text{D4})$$

Following a similar process, we can obtain the corresponding relations for V_{ISHE} arising out $h_{\text{rf},x}$, $h_{\text{rf},y}$, and $h_{\text{rf},z}$ as follows:

$$V_{\text{ISHE},h_x} = A \frac{h_{\text{rf},x}^2}{4} (\sin^2 \theta + \cos^2 \theta \sin^2 \varphi) \cos \varphi \cos \theta, \quad (\text{D5})$$

$$V_{\text{ISHE},h_y} = A \frac{h_{\text{rf},y}^2}{4} (\sin^2 \theta + \cos^2 \theta \cos^2 \varphi) \cos \varphi \cos \theta, \quad (\text{D6})$$

$$V_{\text{ISHE},h_z} = A \frac{h_{\text{rf},z}^2}{4} \cos \varphi \cos^3 \theta. \quad (\text{D7})$$

APPENDIX E: OERSTED FIELD DISTRIBUTION IN Ta/CoFeB/MgO/Al₂O₃ MULTILAYER STRIPS

To understand the Oersted field caused by an induced current when a microwave voltage is applied to the sample, we calculated the magnetic field distribution using the FEM with COMSOL multiphysics simulator. For simplicity, the

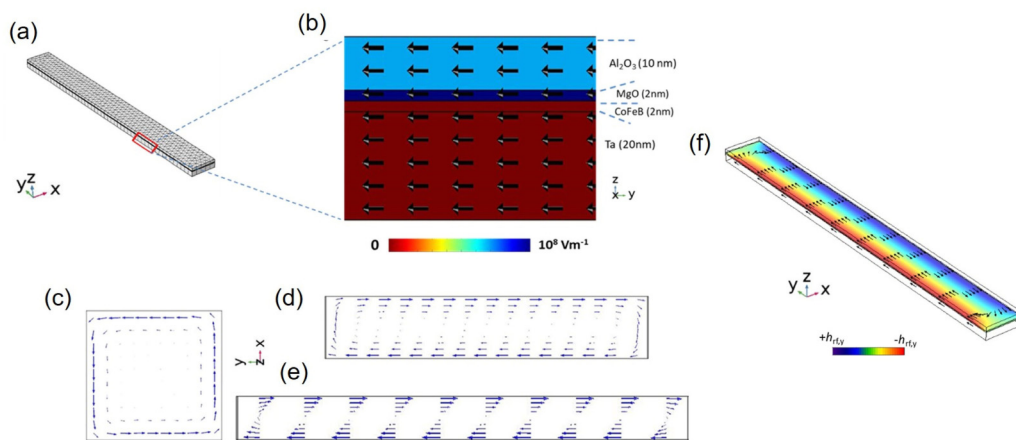


FIG. 10. (a) 20 nm Ta/2 nm CoFeB/2 nm MgO/10 nm Al₂O₃ multilayer structure with size $1 \times 0.1 \mu\text{m}^2$ discretized into triangular mesh elements of size ~ 10 nm. (b) Electric field distribution in the multilayer structure when a power of $10 \mu\text{W}$ is applied on the top surface is color coded as a function of thickness, while the corresponding magnetic field is shown as arrows. Normalized Oersted field distribution (arrows) is shown for samples with $l : w =$ (c) 1:1, (d) 1:5, and (e) 1:10. (f) The microwave field direction (arrows) and amplitude of $h_{\text{rf},y}$ (color scale) in case of a sample with same $l : w$ as the experimental device, i.e., 1:12.

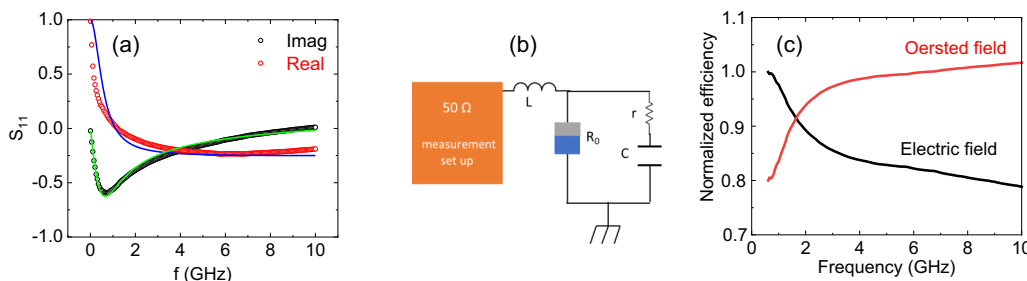


FIG. 11. (a) Typical S_{11} spectra of the sample in this paper. Lines are fits to the experimental data using $S_{11} = \frac{Z-50\ \Omega}{Z+50\ \Omega}$. (b) Schematic of the equivalent circuit of the sample in this measurement. (c) Normalized efficiencies calculated for the electric field torque and the Oersted field torque as a function of frequency of P_{in} .

Ta(5 nm)/Ru(10 nm)/Ta(5 nm) buffer layer has been taken in the form of a single heavy metal layer of 20 nm Ta. As shown in Fig. 10(a), the calculated sample size has been assumed to be $0.1 \times 1\ \mu\text{m}^2$. The mesh grids were taken as triangular elements with a dimension of ~ 10 nm on a side. The input microwave signal of $f = 3$ GHz is applied at a power of $10\ \mu\text{W}$ on the upper Al_2O_3 surface, while the bottom Ta surface is grounded. The applied power is 10^4 times smaller than the actual input power because the calculated sample size is 10^4 times smaller than the actual sample. Figure 10(b) shows the color-coded electric field intensity as a function of the thickness. Additionally, the magnetic field distribution is observed to be along the longer axis of the sample, as shown by arrows in the same diagram. We confirm this behavior by checking the Oersted field distribution in the samples with different length l and width w ratios, as shown in Figs. 10(c)–10(e). Contributions from the z -axial Oersted field h_z can be completely neglected in our samples. Moreover, as $l : w$ increases, the component of Oersted field h along the longer axis increases, i.e., $h_y \gg h_x$.

APPENDIX F: ESTIMATION OF CONTRIBUTIONS OF ELECTRIC FIELD AND OERSTED FIELD TORQUES FROM IMPEDANCE MEASUREMENT

The reflection coefficient S_{11} of the samples was measured using a vector network analyzer. Typical S_{11} spectra in this paper are shown in Fig. 11(a). To estimate the impedance of the CoFeB/MgO junction, we assume an equivalent circuit which is the same as the model for the electric field induced FMR study reported by Nozaki *et al.* [23], as shown in Fig. 11(b). The S_{11} spectra are fitted using the expression $S_{11} = \frac{Z-50\ \Omega}{Z+50\ \Omega}$. Here, $50\ \Omega$ is the characteristic impedance of the measurement setup, while Z is the net impedance obtained from the sample with inductive component L , resistance R_0 , and capacitance C of the junction, and r is the resistive loss between the top and bottom electrodes. From the experimental data, we can see that the Real $[S_{11}] \rightarrow 1$ when frequency $\rightarrow 0$. This indicates a very high value of R_0 because of the 2-nm-thick MgO and 10-nm-thick Al_2O_3 layers in the sample. The S_{11} spectrum in Fig. 11(a) is fitted using $R_0 = 10^5\ \Omega$, $r = 30\ \Omega$, $C = 3.5\ \text{pF}$, and $L = 70\ \text{pH}$.

Using the S_{11} spectra, we can estimate the contributions of the electric field torque and the Oersted field torque as a func-

tion of f for the sample. In the case of the electric field torque, the voltage applied to the sample is expressed as $V \propto (1 + S_{11})V_{input} = \zeta_V V_{input}$. In the case of the Oersted field torque, the current is proportional to the square root of the power inserted into the sample, as $I \propto \sqrt{P} = \sqrt{(1 - |S_{11}|^2)P_{in}} = \zeta_I \sqrt{P_{in}}$. The efficiency of the electric field torque decreases with increasing f , whereas the efficiency of the Oersted field torque increases with increasing f , as shown in Fig. 11(c).

APPENDIX G: ANGULAR DEPENDENCE OF INVERSE SPIN HALL VOLTAGE IN HIGHER FREQUENCIES

We performed in-plane angle-dependent measurements of the inverse spin Hall voltage V_{ISHE} with different microwave frequencies. Figure 12(a) shows the V_{ISHE} for frequencies 2 and 4 GHz, at $\theta = 0^\circ$ and 40° and $P_{in} = 0.001\ \text{W}$. The angular-dependent data for $f = 4$ GHz are presented in Fig. 12(b). Upon fitting the data to Eq. (4) of the main text, we obtained values $a(\frac{\partial H_k}{\partial V} V_{\text{rf}})^2 = 0.90$ and $ah_{\text{rf},y}^2 = 0.65$. Note that, from the data in Fig. 5(a), we obtained $a(\frac{\partial H_k}{\partial V} V_{\text{rf}})^2 = 2.87$ and $ah_{\text{rf},y}^2 = 0.88$ for $f = 2$ GHz. It shows that, as frequency increases, the VCMA contribution is reduced, while the Oersted field contribution increases. This further proves the presence of VCMA of H_k in our devices, as can be understood from Appendix F, which shows that their torques have a decreasing and increasing frequency dependence, respectively.

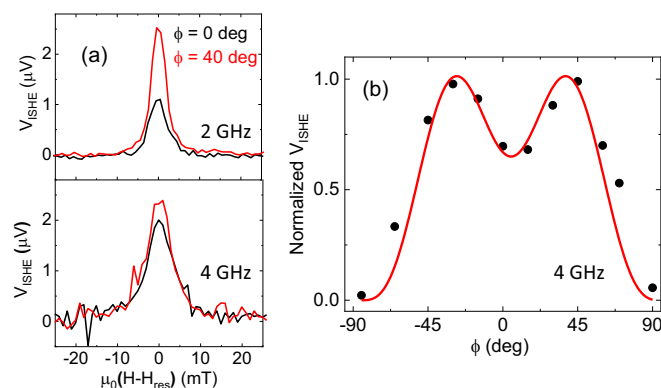


FIG. 12. (a) Rectified voltages for 2 and 4 GHz at $\phi = 0^\circ$ and 40° . (b) Dependence of normalized V_{ISHE} on ϕ for 4 GHz. The experimental data are fitted using Eq. (4).

- [1] L. Appleltant, M. C. Soriano, G. Van der Sande, J. Danckaert, S. Massar, J. Dambre, B. Schrauwen, C. R. Mirasso, and J. Fischer, Information processing using a single dynamical node as complex system, *Nat. Commun.* **2**, 468 (2011).
- [2] J. Torrejon, M. Riou, F. A. Araujo, S. Tsunegi, G. Khalsa, D. Querlioz, P. Bortolotti, V. Cros, K. Yakushiji, A. Fukushima, H. Kubota, S. Yuasa, M. D. Stiles, and J. Grollier, Neuromorphic computing with nanoscale spintronic oscillators, *Nature (London)* **547**, 428 (2017).
- [3] G. Tanaka, T. Yamane, J. B. Heroux, R. Nakane, N. Kanazawa, S. Takeda, H. Numata, D. Nakano, and A. Hirose, Recent advances in physical reservoir computing: A review, *Neural Netw.* **115**, 100 (2019).
- [4] A. G. Gurevich and G. A. Melkov, *Magnetization Oscillation and Waves* (CRC Press, Boca Raton, FL, 1996).
- [5] P. E. Wigen, *Nonlinear Phenomena and Chaos in Magnetic Materials* (World Scientific, Singapore, 1994).
- [6] H. Kurebayashi, O. Dzyapko, V. E. Demidov, D. Fang, A. J. Ferguson, and S. O. Demokritov, Controlled enhancement of spin-current emission by three-magnon splitting, *Nat. Mater.* **10**, 660 (2011).
- [7] C. W. Sandweg, Y. Kajiwara, A. V. Chumak, A. A. Serga, V. I. Vasyuchka, M. B. Jungfleisch, E. Saitoh, and B. Hillebrands, Spin Pumping by Parametrically Excited Exchange Magnons, *Phys. Rev. Lett.* **106**, 216601 (2011).
- [8] K. Ando and E. Saitoh, Spin Pumping Driven by Bistable Exchange Spin Waves, *Phys. Rev. Lett.* **109**, 026602 (2012).
- [9] A. Yu. Dobin and R. H. Victora, Intrinsic Nonlinear Ferromagnetic Relaxation in Thin Metallic Films, *Phys. Rev. Lett.* **90**, 167203 (2003).
- [10] T. Gerrits, P. Krivosik, M. L. Schneider, C. E. Patton, and T. J. Silva, Direct Detection of Nonlinear Ferromagnetic Resonance in Thin Films by the Magneto-Optical Kerr Effect, *Phys. Rev. Lett.* **98**, 207602 (2007).
- [11] Y. S. Gui, A. Wirthmann, N. Mecking, and C.-M. Hi, Direct measurement of nonlinear ferromagnetic damping via the intrinsic foldover effect, *Phys. Rev. B* **80**, 060402(R) (2009).
- [12] J. S. Slonczewski, Current-driven excitation of magnetic multilayers, *J. Magn. Magn. Mater.* **159**, L1 (1996).
- [13] L. Berger, Emission of spin waves by a magnetic multilayer traversed by a current, *Phys. Rev. B* **54**, 9353 (1996).
- [14] I. M. Miron, K. Garello, G. Gaudin, P.-J. Zermatten, M. V. Costache, S. Auffret, S. Bandiera, B. Rodmacq, A. Schuhl, and P. Gambardella, Perpendicular switching of a single ferromagnetic layer induced by in-plane current injection, *Nature (London)* **476**, 189 (2011).
- [15] M. Weisheit, S. Fähler, A. Marty, Y. Souche, C. Poinsignon, and D. Givord, Electric field-induced modification of magnetism in thin-film ferromagnets, *Science* **315**, 4349 (2007).
- [16] C.-G. Duan, J. P. Velev, R. F. Sabirianov, Z. Zhu, J. Chu, S. S. Jaswal, and E. Y. Tsymlal, Surface Magnetoelectric Effect in Ferromagnetic Metal Films, *Phys. Rev. Lett.* **101**, 137201 (2008).
- [17] T. Maruyama, Y. Shiota, T. Nozaki, K. Ohta, N. Toda, M. Mizuguchi, A. A. Tulapurkar, T. Shinjo, M. Shiraishi, S. Mizukami, Y. Ando, and Y. Suzuki, Large voltage-induced magnetic anisotropy change in a few atomic layers of iron, *Nat. Nanotechnol.* **18**, 158 (2009).
- [18] F. Matsukura, Y. Tokura, and H. Ohno, Control of magnetism by electric fields, *Nat. Nanotechnol.* **10**, 209 (2015).
- [19] R. Verba, V. Tiberkevich, I. Krivorotov, and A. Slavin, Parametric Excitation of Spin Waves by Voltage-Controlled Magnetic Anisotropy, *Phys. Rev. Applied* **1**, 044006 (2014).
- [20] Y. J. Chen, H. K. Lee, R. Verba, J. A. Katine, I. Barsukov, V. Tiberkevich, J. Q. Xiao, A. N. Slavin, and I. N. Krivorotov, Parametric resonance of magnetization excited by electric field, *Nano Lett.* **17**, 572 (2017).
- [21] P. Bruno, Tight-binding approach to the orbital magnetic moment and magnetocrystalline anisotropy of transition-metal monolayers, *Phys. Rev. B* **39**, 865 (1989).
- [22] H. X. Yang, M. Chshiev, B. Dieny, J. H. Lee, A. Manchon, and K. H. Shin, First-principles investigation of the very large perpendicular magnetic anisotropy at Fe|MgO and Co|MgO interfaces, *Phys. Rev. B* **84**, 054401 (2011).
- [23] T. Nozaki, Y. Shiota, S. Miwa, S. Murakami, F. Bonell, S. Ishibashi, H. Kubota, K. Yakushiji, T. Takeshi, T. Saruya, A. Fukushima, S. Yuasa, T. Shinjo, and Y. Suzuki, Electric-field-induced ferromagnetic resonance excitation in an ultrathin ferromagnetic metal layer, *Nat. Phys.* **8**, 491 (2012).
- [24] J. Zhu, J. A. Katine, G. E. Rowlands, Y.-J. Chen, Z. Duan, J. G. Alzate, P. Upadhyaya, J. Langer, P. K. Amiri, K. L. Wang, and I. N. Krivorotov, Voltage-Induced Ferromagnetic Resonance in Magnetic Tunnel Junctions, *Phys. Rev. Lett.* **108**, 197203 (2012).
- [25] S. Kanai, M. Gajek, D. C. Worledge, F. Matsukura, and H. Ohno, Electric field-induced ferromagnetic resonance in a CoFeB/MgO magnetic tunnel junction under dc bias voltages, *Appl. Phys. Lett.* **105**, 242409 (2014).
- [26] E. Hirayama, S. Kanai, J. Ohe, H. Sato, F. Matsukura, and H. Ohno, Electric-field induced nonlinear ferromagnetic resonance in a CoFeB/MgO magnetic tunnel junction, *Appl. Phys. Lett.* **107**, 132404 (2015).
- [27] B. Rana, Y. Fukuma, K. Miura, H. Takahashi, and Y. Otani, Effect of excitation power on voltage induced local magnetization dynamics in an ultrathin CoFeB film, *Sci. Rep.* **7**, 2318 (2017).
- [28] K. Miura, S. Yabuuchi, M. Yamada, M. Ichimura, B. Rana, S. Ogawa, H. Takahashi, Y. Fukuma, and Y. Otani, Voltage-induced magnetization dynamics in CoFeB/MgO/CoFeB magnetic tunnel junctions, *Sci. Rep.* **7**, 42511 (2017).
- [29] A. Deka, B. Rana, K. Miura, H. Takahashi, Y. Otani, and Y. Fukuma, Electric-field control of interfacial in-plane magnetic anisotropy in CoFeB/MgO junctions, *Phys. Rev. B* **101**, 174405 (2020).
- [30] E. Schlomann, J. J. Green, and U. Milano, Recent developments in ferromagnetic resonance at high power levels, *J. Appl. Phys.* **31**, S386 (1960).
- [31] G. Wiese, L. Buxman, P. Kabos, and C. E. Patton, Parallel pumping fine structure at 9.4 GHz for in-plane magnetized yttrium iron garnet thin films, *J. Appl. Phys.* **75**, 1041 (1993).
- [32] S. Y. An, P. Krivosik, M. A. Kraemer, H. M. Olson, A. V. Nazarov, and C. E. Patton, High power ferromagnetic resonance and spin wave instability processes in Permalloy thin films, *J. Appl. Phys.* **96**, 1572 (2004).
- [33] F. Guo, L. M. Belova, and R. D. McMichael, Nonlinear ferromagnetic resonance shift in submicron Permalloy ellipses, *Phys. Rev. B* **91**, 064426 (2015).
- [34] J. Lustikova, Y. Shiomi, Y. Hanada, and E. Saitoh, Spectral shape deformation in inverse spin Hall voltage in Y3Fe5O12/Pt bilayers at high microwave power levels, *J. Appl. Phys.* **117**, 073901 (2015).

- [35] A. Deka, I. Tanaka, J. Mohan, and Y. Fukuma, Modulation of magnetization precession trajectories by perpendicular magnetic anisotropy in CoFeB thin films, *IEEE Trans. Magn.* **56**, 1 (2020).
- [36] A. Houshang, R. Khymyn, H. Fulara, A. Gangwar, M. Haidar, S. R. Etesami, R. Ferreira, P. P. Freitas, M. Dvornik, R. K. Dumas, and J. Ackerman, Spin transfer torque driven higher-order propagating spin waves in nanocontact magnetic tunnel junctions, *Nat. Commun.* **9**, 4374 (2018).
- [37] H. M. Olson, P. Krivosik, K. Srinivasan, and C. E. Patton, Ferromagnetic resonance saturation and second order Suhl spin wave instability processes in thin Permalloy films, *J. Appl. Phys.* **102**, 023904 (2007).
- [38] Y. Tserkovnyak, A. Brataas, and G. E. W. Bauer, Spin pumping and magnetization dynamics in metallic multilayers, *Phys. Rev. B* **66**, 224403 (2002).
- [39] O. Mosendz, V. Vlamincik, J. E. Pearson, F. Y. Fradin, G. E. W. Bauer, S. D. Bader, and A. Hoffmann, Detection and quantification of inverse spin Hall effect from spin pumping in permalloy/normal metal bilayers, *Phys. Rev. B* **82**, 214403 (2010).
- [40] S. Gupta, R. Medwal, D. Kodama, K. Kondou, Y. Otani, and Y. Fukuma, Important role of magnetization precession angle measurement in inverse spin Hall effect induced by spin pumping, *Appl. Phys. Lett.* **110**, 022404 (2017).
- [41] H. Suhl, The theory of ferromagnetic resonance at high signal powers, *J. Phys. Chem. Solids* **1**, 209 (1957).
- [42] C. Bi, Y. Liu, T. N. Illige, M. Xu, M. Rosales, J. W. Freeland, O. Mryasov, S. Zhang, S. G. E. te Velthuis, and W. G. Wang, Reversible Control of Co Magnetism by Voltage-Induced Oxidation, *Phys. Rev. Lett.* **113**, 267202 (2014).
- [43] V. B. Naik, H. Meng, J. X. Xiao, R. S. Liu, A. Kumar, K. Y. Zeng, P. Luo, and S. Yap, Effect of electric-field on the perpendicular magnetic anisotropy and strain properties in CoFeB/MgO magnetic tunnel junctions, *Appl. Phys. Lett.* **105**, 052403 (2014).
- [44] B. Rana and Y. Otani, Towards magnonic devices based on voltage-controlled magnetic anisotropy, *Commun. Phys.* **2**, 90 (2019).
- [45] R. Medwal, A. Deka, J. V. Vas, M. Duchamp, H. Asada, S. Gupta, Y. Fukuma, and R. S. Rawat, Facet controlled anisotropic magnons in $Y_3Fe_5O_{12}$ thin films, *Appl. Phys. Lett.* **119**, 162403 (2021).
- [46] M. Harder, Y. Gui, and C-M. Hu, Electrical detection of magnetization dynamics via spin rectification effects, *Phys. Rep.* **661**, 1 (2016).